Visualization of viscous and quantum flows of liquid ^{4}He due to an oscillating cylinder of rectangular cross section

D. Duda, P. Švančara, M. La Mantia,[*] M. Rotter, and L. Skrbek

Faculty of Mathematics and Physics, Charles University, Ke Karlovu 3, 121 16 Prague, Czech Republic

The motions of micrometer-sized solid deuterium particles in liquid ^{4}He, at temperatures between approximately 1.2 and 3 K, are visualized in the proximity of an oscillating cylinder of rectangular cross section (3 mm high and 10 mm wide). The cylinder is oscillating vertically, perpendicularly to its cross-section width, at frequencies between 0.05 and 1.25 Hz, and amplitudes of 5 and 10 mm, resulting in Reynolds numbers Re up to 10^5. The aim of the reported experiments is to investigate systematically the macroscopic vortical structures shed at the cylinder sharp edges, by tracking the deuterium particles. We find that large-scale, millimeter-sized vortices are generated in the surrounding fluid by the oscillating cylinder, both in viscous He I and superfluid He II. An estimate of the strength of the shed vortical structures reveals that, for $Re > 10^4$, the corresponding magnitudes are approximately equal in He I and He II if, in He II, the kinematic viscosity is suitably defined. For $Re < 10^4$, the strength of the large-scale vortices is smaller in He II than in He I. Although the outcome is partly affected by the larger scatter of the He I data and possibly also by the much larger heat conductivity of superfluid ^{4}He, we argue that the fundamental physical reason for observing this difference is that, at these Reynolds numbers, the experimentally probed length scales in He II are smaller than the average distance between quantized vortices—the quantum length scale of the flow. The result strongly suggests that, similarly to thermal counterflow, both viscous and quantum features can be observed in mechanically driven flows of He II, depending on the length scales at which the quantum flow is probed.

I. INTRODUCTION

Quantum turbulence [1,2], often defined as the most general form of motion of quantum fluids displaying superfluidity, such as superfluid ^{4}He, is the focus of an active and challenging line of scientific research that combines quantum physics with fluid mechanics. Below the superfluid transition temperature $T_\lambda \approx 2.17$ K and above approximately 1 K, at the saturated vapor pressure, superfluid ^{4}He, also known as He II, displays the two-fluid behavior and, on the phenomenological level, can be viewed as consisting of two interpenetrating fluids, whose density ratio depends on temperature. The viscous normal component, which carries the entire entropy content of the quantum fluid, represents the gas of thermal excitations, while the superfluid component is assumed inviscid and its circulation is quantized in units of the quantum of circulation $\kappa = h/m = 9.97 \times 10^{-8}$ m^2/s [3], where h is the Planck constant and m denotes the mass of the ^{4}He atom.

Quantized vortices—line singularities within the superfluid—can consequently exist in He II and are usually arranged in a tangle, whose dynamical behavior is an essential ingredient of quantum turbulence. The existence of such vortices constitutes indeed one of the most notable differences between quantum and viscous flows, as the strength of the vortices occurring in the latter is not quantized but can vary continuously.

In the past few years, deeper understanding of the two-fluid hydrodynamics of He II has been achieved by visualizing the motions of relatively small particles seeding the flows of interest, see, e.g., the recent review by Guo *et al.* [4]. The particles, suspended in the fluid, reflect the light of an appropriate source, for example, a laser sheet, and their time-dependent positions are captured, e.g., by a digital camera. The just outlined experimental method allows therefore the study of the particle dynamics within the fluid and consequently reveals the underlying flow-induced physics.

Fundamental results in the investigation of two-fluid flows of He II have been obtained by tracking solid hydrogen and deuterium particles of micrometer size. Their motions are complex, as particles interact with both the normal and superfluid velocity fields simultaneously, the corresponding dynamics being additionally influenced by that of quantized vortices. In other words, from the observed particle motions it is possible to shed light on the behavior of superfluid ^{4}He flows but, at present, it is generally difficult to discern the contributions to the particle dynamics originating independently from the two postulated flow fields. Nevertheless, the application of visualization techniques to He II flows, seeded with these particles, resulted in the discovery of nonclassical velocity statistics in thermal counterflow [5–7], among other results, such as observations of quantized vortex reconnections [8] and of forced (mechanically driven) flows past a circular cylinder [9]. Recently, we have reported the crossover between viscous and quantum features in the particle velocity and acceleration distributions, obtained in thermal counterflow, probed simultaneously at various length scales, larger and smaller than the quantum length scale of the flow, determined by the averaged distance between quantized vortices [10,11].

Flows of He II due to oscillating structures (which are widely used in quantum turbulence research since the discovery of superfluidity, see, e.g., Refs. [12,13] and references therein) have not been extensively investigated by visualization methods to date. This is despite the fact that the latter techniques, as already testified by supporting experiments performed in Prague [14,15] and by the qualitative results

---

[*]lamantia@nbox.troja.mff.cuni.cz

of Luzuriaga *et al.* [16,17], appear adequate to analyze such important flows of liquid ^{4}He, in order, for example, to clarify the mechanisms of vortex generation at the oscillator edges. The present work aims at giving a meaningful contribution to this promising line of scientific enquiry by visualizing the flow in the proximity of a cylinder of rectangular cross section, oscillating in the quiescent liquid. Such a shape of the oscillator was specifically chosen due to its similarity to the shape of quartz tuning forks, the most common oscillators presently employed in quantum turbulence studies [12,18], and to enhance the possibility of observing large-scale vortices, compared to a circular cross section.

More generally, the paper reports a systematic visualization study of the occurrence of macroscopic vortices in quantum flows, which, to the best of our knowledge, was not performed previously, although large-scale vortical structures in flows of superfluid ^{4}He have been already visualized, in the form of vortex rings, by Murakami *et al.* [19], for a mechanically generated flow, and by Stamm *et al.* [20], for a thermally driven jet flow; see also the influential work by Zhang and Van Sciver [21] on thermal counterflow past a circular cylinder.

In the field of fluid dynamics, investigations of viscous flows past cylinders, which are relevant to that reported here, constitute one of the most popular research topics, see, e.g., the review by Williamson [22]. More specifically, these studies are often focused on establishing relations, if any, between the observed vortical wakes and the flow-induced forces acting on the bluff bodies, as it is customary for similar investigations on oscillating wings [23,24]. Studies on cylinders of rectangular cross section accelerating in a quiescent viscous fluid are, however, scarce, compared to those on circular cylinders, and the present work can also be seen as belonging to the former field of research, which includes the investigations performed by Taneda and Honji [25], on the unsteady flow past a flat plate, by Tao and Thiagarajan [26], on the flow generated by an oscillating sharp-edged cylinder, and by Phan *et al.* [27], on vibrating cantilevers.

Two nondimensional parameters are frequently used in the literature to characterize oscillatory viscous flows in the proximity of bodies having the same geometry [28]. The Keleugan-Carpenter number K_C is defined as

$$K_C = \frac{2\pi a}{D}, \tag{1}$$

where a denotes the oscillation amplitude and D is a characteristic dimension of the body (which, in the case of a circular cylinder, can be the diameter). K_C indicates therefore how large the imposed body oscillations are, compared to its size. The Stokes number β can be seen as a measure of the motion unsteadiness and is usually written as

$$\beta = \frac{fD^2}{\nu}, \tag{2}$$

where f denotes the oscillation frequency, in hertz, and ν is the fluid kinematic viscosity. Besides, β is proportional to the squared ratio of the characteristic dimension D and the viscous penetration depth δ, which can be written as $\sqrt{\nu/\omega}$ and is assumed to be the thickness of the layer close to the moving object where viscous effects are important ($\omega = 2\pi f$ indicates the angular oscillation frequency, in s^{-1}). Note also

that, as discussed below, the kinematic viscosity of He II cannot be defined unequivocally and that, additionally, various definitions of effective kinematic viscosity have been proposed for He II flows, see, e.g., Refs. [29,30].

The product of K_C and β represents the Reynolds number Re, that is,

$$Re = \frac{\omega a D}{\nu} = \frac{aD}{\delta^2}, \tag{3}$$

where ωa can be understood as the velocity amplitude in the case of harmonic oscillations. As mentioned above, we have to bear in mind that the just introduced nondimensional numbers can only be used to compare oscillations of objects having the same geometry. In other words, results obtained for oscillating circular cylinders cannot be straightforwardly extended to wings or cylinders of rectangular cross section. Additional parameters should be added to characterize and compare the corresponding flows, such as the thickness to width ratio [26] or the wing section shape [23,24].

II. EXPERIMENTAL APPARATUS

We use the cryogenic visualization setup described in our previous publications, see Ref. [11] and references therein; its main component is a low-loss, custom-built cryostat with an optical tail, which constitutes our experimental volume. The latter is approximately 300 mm long and has a square cross section of 50 mm sides. An optical port, of 25 mm diameter, is placed on each of the four tail sides, at 100 mm from the tail bottom. The temperature of the ^{4}He bath is regulated by controlling the pumping rate of the helium vapor (the corresponding pressure is used for deducing the temperature, based on the saturated-vapor-pressure curve).

A purpose-made seeding system generates the solid deuterium particles. They are obtained by mixing helium and deuterium gasses at room temperature, in a volume ratio of approximately 100 to 1, respectively, and by suitably injecting the mixture into the liquid, as gaseous deuterium solidifies during the injection, at about 19 K [31]. The particle diameter is usually smaller than 10 μm, see Ref. [10] for typical particle size distributions, and their density is 200 kg/m^3 [32], i.e., solid deuterium is appreciably denser than liquid ^{4}He. The illumination of the flow field is provided by a continuous-wave, solid-state laser, whose power does not exceed 0.1 W during the experiments [33]. A thin laser sheet, less than 1 mm thick, is obtained using adequate cylindrical optics (the sheet leaves the experimental volume through the optical port opposite to the one through which it goes inside). A CMOS camera, situated perpendicularly to the laser sheet, is sharply focused, by the means of a macro lens, on a 34.1 mm (1200 px) wide and 21.4 mm (800 px) high field of view, placed as far as possible from the flow boundaries, in order to collect the illuminated particle positions (three optical ports are therefore presently employed, two, on opposite sides of the tail, for the laser and one for the camera).

The moving obstacle (see the left panel of Fig. 1) has a rectangular cross section 3 mm high and 10 mm wide, and is 30 mm long (the laser sheet illuminates the middle part of the cylinder length, which is in the horizontal direction). The cylinder is made of transparent plexiglass in order to
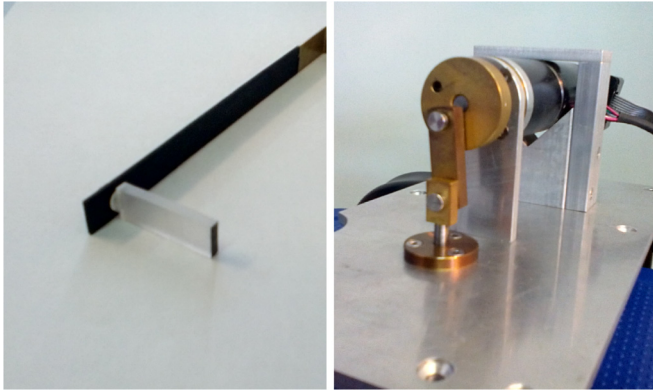
FIG. 1. (Color online) (Left) Picture of the 30 mm long plexiglass cylinder of rectangular cross section (3 mm high and 10 mm wide) and of the bottom part of its brass support. The cylinder section facing the camera and the bottom part of the support are painted in black to reduce possible laser-induced reflections. (Right) Picture of the step motor and of the crank mechanism, connected, on top of the cryostat, to the stainless steel shaft firmly linked to the top part of the cylinder support.

avoid the generation of thermal counterflow at the obstacle surface, as it was reported to happen for the heated surface of a circular cylinder made of metal [33]. The obstacle is supported vertically at one of its ends (the one further away from the camera) in such a way that the walls of the cylinder are parallel to those of the cryostat optical tail. The upper part of the brass support is firmly connected to a stainless steel shaft, of 5 mm diameter, which allows the transmission of the imposed motion.

The shaft exits the low-temperature volume of the cryostat through a narrow channel, sealed, on both ends, by rubber o-rings against the shaft. An overpressure of gaseous helium in this channel ensures that the cryostat is insulated from any room-temperature air leakage. The shaft is connected to a computer-controlled motor placed on top of the cryostat. A purpose-made crank mechanism (see the right panel of Fig. 1) transmits the rotational motion generated by the step motor to the vertical shaft connected to the rectangular cylinder, enabling therefore the cylinder vertical oscillations. The imposed motion is a quasiharmonic one due to the crank mechanism, i.e., it cannot be expressed as a simple sine or cosine function but it is very similar to a harmonic motion. Additionally, it is ensured that the cylinder is always visible by the camera when it reaches the lowest position of its oscillating cycle (the same does not apply to the cylinder uppermost position).

III. EXPERIMENTAL PROTOCOL AND DATA PROCESSING

The cylinder oscillates in liquid ^{4}He at temperatures between approximately 1.2 and 3 K, at the saturated vapor pressure. The vertical oscillations, perpendicular to the cylinder cross-section width, have frequencies between 0.05 and 1.25 Hz, and amplitudes of 5 and 10 mm, resulting in Reynolds numbers up to 10^5 (the characteristic obstacle size D is set to the cylinder width, i.e., $D = 10$ mm).

Above T_λ, liquid ^{4}He is called He I and behaves as a viscous fluid, characterized by extremely low values of kinematic viscosity, about three orders of magnitude smaller than those of air, tabulated, together with other fluid properties, in Ref. [3]. It is therefore straightforward to calculate the (viscous) Reynolds number Re from Eq. (3).

The kinematic viscosity of He II cannot be defined unequivocally. Here, we use two different definitions of ν, reported in the literature, which are generally assumed to be valid depending on whether the probed length scale exceeds or is of the order of the average distance between quantized vortices, i.e., if the flows of the two components of He II can be considered locked together by the action of the mutual friction force.

The first definition we use is often employed to characterize forced flows of He II, see, e.g., Refs. [9,34], as it is similar to that customary for viscous fluids. The kinematic viscosity ν is set equal to μ_n/ρ, where μ_n denotes the normal component dynamic viscosity and ρ is the total density of the fluid, which are also tabulated in Ref. [3]. The relevant (viscouslike) Reynolds number is consequently calculated as

$$Re_n = \frac{\rho \omega a D}{\mu_n}. \tag{4}$$

The second definition of ν we employ here to characterize the obtained He II data follows from the recent work by L'vov *et al.* [30] (see below the related discussion). We accordingly decided to use the value $\nu = \kappa/6$ for computing the corresponding (superfluid) Reynolds number as

$$Re_\kappa = \frac{6 \omega a D}{\kappa}, \tag{5}$$

where $\kappa/6 = 1.66 \times 10^{-8}$ m^2/s.

In each experimental condition, defined by temperature T, frequency f, and amplitude a, 2000 images are captured by the camera, at 100 fps. The 20-s-long movies are taken in such a way that residual flows, due, for example, to particle injection in He I, are minimized and that enough particles are visible in the field of view, i.e., the cylinder motion is imposed for at least 45 s before collecting images.

Once the movies are stored, the first step of the data processing procedure is to mask the over-lighted obstacle, to reduce the related noise, by using a custom-made computer program. The images are subsequently cropped in order to eliminate the out-of-focus edges of the cryostat window. The resulting images are 21.4 mm (800 px) wide and 16.0 mm (600 px) high, for $a = 5$ mm, and 21.4 mm (800 px) wide and 21.4 mm (800 px) high, for $a = 10$ mm. Particle positions and trajectories are then computed by using an open-source tracking algorithm [35] and the corresponding particle velocities are obtained linearly from the particle positions by the means of another code, developed by us [7,36].

In order to take advantage of the periodic character of the imposed motion and to enhance the statistical quality of our data, the calculated particle tracks are phase averaged. More specifically, data obtained within the same phase interval of the periodic motion are merged in such a way that particle trajectories, which depend on time, become function of the phase interval too (note that the initial phase of the motion is
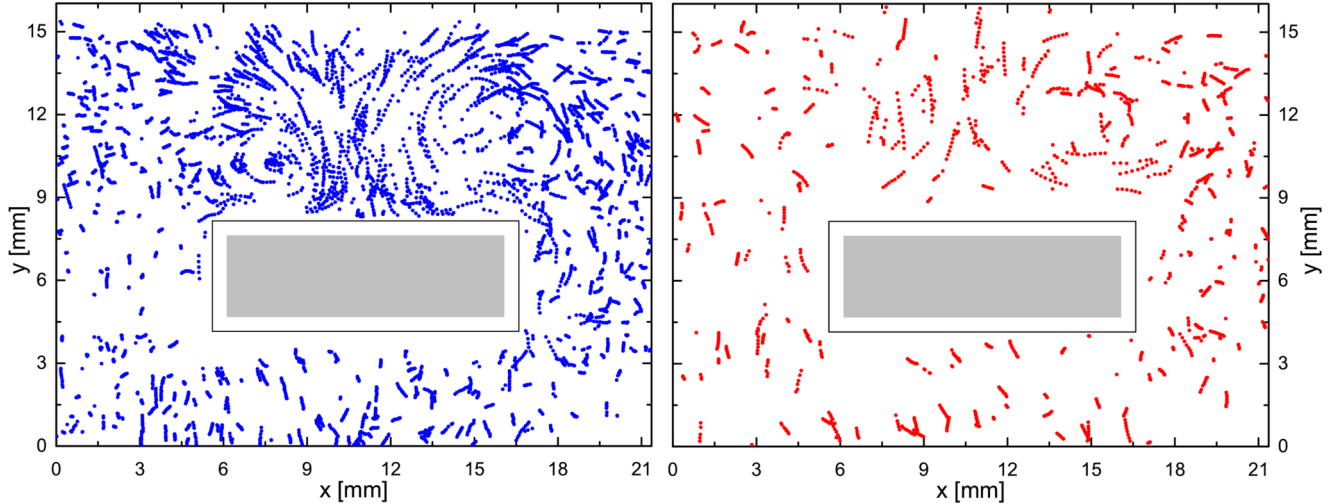
FIG. 2. (Color online) Particle trajectories, with at least five points, obtained within the 15° phase interval centered at the lowest position of the cylinder oscillatory motion; frequency $f = 0.5$ Hz and amplitude $a = 5$ mm; 21.4 mm wide and 16.0 mm high field of view. (Left) He II, temperature $T = 1.24$ K, Reynolds numbers $Re_n = 11\ 717$, Eq. (4), and $Re_\kappa = 9428$, Eq. (5). (Right) He I, $T = 2.18$ K and Reynolds number $Re = 9092$, Eq. (3). The grey rectangles indicate the cylinder, at the lowest position of the cycle, while the white rectangles denote the corresponding mask used for data processing. See the text for further details on the three definitions of the Reynolds number.

not the same in all the collected movies and that usually each movie contains more than one cycle of oscillations).

IV. RESULTS

Figure 2 displays typical particle trajectories obtained following the procedure just outlined, within the 15° phase interval centered at the lowest position of the oscillating cycle, at frequency $f = 0.5$ Hz and amplitude $a = 5$ mm. Pairs of macroscopic fluid vortices of size comparable to the cylinder width can be inferred from the observed trajectories of deuterium particles, both in He I (right) and He II (left). The vortical structures seem to be similar to those observed in the proximity of flat plates accelerating in viscous fluids [25]. However, as discussed below, the large-scale vortices generated in He II appear to be more evident than the vortical structures shed in He I.

It was chosen to keep for further processing only trajectories with at least five points, consistently with our previous studies, see Ref. [11] and references therein. This led, for specific experimental conditions, i.e., for each processed movie, to a total number of track points equal to at least 6300 and up to approximately 162 000.

A. Vortex strength

Unsteady flows of viscous fluids can often be characterized by the vorticity, as reported, e.g., in Refs. [26,27]. This (local) quantity can be seen as a measure of the vortex strength in the flow field of interest and is calculated from the spatial derivatives of the fluid velocity as

$$\boldsymbol{\Omega} = \nabla \times \mathbf{v}, \qquad (6)$$

where $\boldsymbol{\Omega}$ indicates the flow vorticity vector and $\mathbf{v}$ denotes the fluid velocity vector. The vorticity cannot consequently be computed in our case, due to the fact that the fluid velocity is

not known everywhere at a given time, as shown, for example, in Fig. 2.

In order to quantify the magnitude of the shed vortices, we introduce the parameter θ, which is loosely related to the flow vorticity and is defined as

$$\theta(\mathbf{r}, \varphi) = \frac{1}{M} \sum_{i=1}^{M} \frac{[(\mathbf{r}_i - \mathbf{r}) \times \mathbf{v}_i]_z}{|\mathbf{r}_i - \mathbf{r}|^2}, \qquad (7)$$

where $\mathbf{r}$ denotes the position where θ is calculated, on a chosen mesh that covers adequately the field of view; similarly, φ is the phase of the oscillatory motion at which the computation is performed; $\mathbf{r}_i$, $\mathbf{v}_i$, and ϕ_i indicate the position, velocity, and phase of the ith particle, respectively, within the spatial region of radius R_M, centered in $\mathbf{r}$, and in the phase interval equal to 2Φ, centered in φ. M is the total number of considered trajectory points and the subscript z denotes that only the out-of-plane component of the vector $[(\mathbf{r}_i - \mathbf{r}) \times \mathbf{v}_i]$ is used to obtain the (scalar) parameter θ.

We ought to emphasize at this point that we see a single velocity field, that of the visualized particles. As mentioned above, the contributions to the particle dynamics originating independently from the two postulated flow fields of He II are at present difficult to separate, as the used deuterium particles, which are not tracers (i.e., fluid particles), generally interact simultaneously with both velocity fields and their motions are additionally influenced by those of quantized vortices.

The rectangular mesh having one point every 10 px in both directions was found to give results independent on the mesh size. The radius R_M was set to 5 mm, which corresponds to the approximate diameter of the visualized vortices, and the phase parameter Φ was chosen to be equal to 7.5°, as this allows to observe adequately the generated vortical structures, see again Fig. 2.

Note that the term $|\mathbf{r}_i - \mathbf{r}|^2$ in the denominator of Eq. (7) is introduced to account for the fact that both the number of included trajectory points and the relevant vector product scale
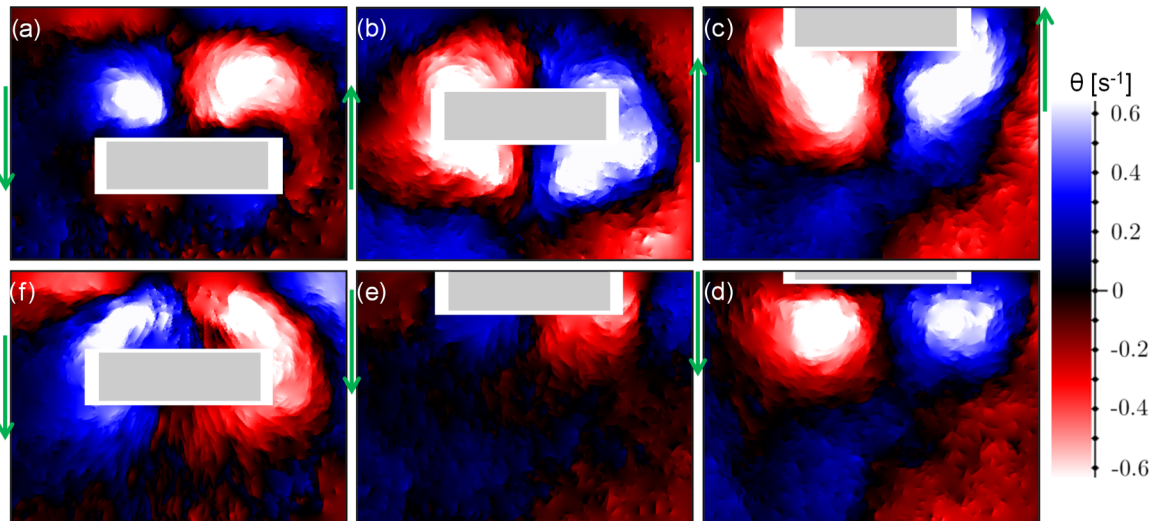
FIG. 3. (Color online) Maps of the $\theta(\mathbf{r}, \varphi)$ parameter for (clockwise, from the top left panel) phase $\varphi = 90° \pm 7.5°$ (a), $150° \pm 7.5°$ (b), $210° \pm 7.5°$ (c), $270° \pm 7.5°$ (d), $330° \pm 7.5°$ (e), and $30° \pm 7.5°$ (f). Temperature $T = 1.24$ K, frequency $f = 0.5$ Hz, and amplitude $a = 5$ mm. The grey rectangles indicate the cylinder positions, in the middle of the considered phase intervals, while the white rectangles denote the corresponding masks used for data processing. The green arrows between the panels show the direction of motion, e.g., in panel (a) the cylinder is at the lowest position of the cycle, see also the left panel of Fig. 2.

linearly with the magnitude of **r**. The parameter $\theta(\mathbf{r}, \varphi)$ has consequently the same dimensions as the vorticity, i.e., s^{-1}, and can be seen as a measure of the vortex strength. Besides, it can be derived that, in the limits $R_M \to 0$ and $\Phi \to 0$, for a large enough number of fluid particles, $\theta(\mathbf{r}, \varphi)$ would indeed represent the flow vorticity.

In Fig. 3, maps of the $\theta(\mathbf{r}, \varphi)$ parameter are shown, at $T = 1.24$ K, $f = 0.5$ Hz, and $a = 5$ mm, for various phase intervals. The macroscopic vortex pairs shed at the cylinder edges during the cycle are clearly visible. The same applies to Fig. 4, where, additionally, it can be seen that, as the imposed oscillation frequency increases, the magnitude of the generated vortices also increases. Similar results are obtained at $a = 10$ mm and in He I, as displayed in Fig. 5. However, as mentioned above, the vortical structures observed in He I are less clearly defined than those seen in He II.

B. Behavior of $\langle \theta^2 \rangle$

In order to quantify how the magnitude of the shed vortices depends on the experimental conditions, which are temperature T, frequency f, and amplitude a, we compute, for each processed movie, $\langle \theta^2 \rangle$, i.e., the ensemble average of θ^2, because the positive parameter $\langle \theta^2 \rangle$ retains useful quantitative information that allow the comparison of the visualized flow fields. It can be interpreted as the square of the average flow vorticity Ω, coarse-grained over the area of radius R_M, within the phase interval 2Φ, the latter being two characteristic parameters of the studied periodic flows.

While we do not observe any clear temperature dependence of $\langle \theta^2 \rangle$ in He II, in He I it appears to be an increasing function of T. This difference is probably influenced by the larger data scatter in He I, compared to that in He II, especially at low oscillation frequencies. Moreover, as discussed below, this could also be due to other reasons, such as the different heat conductivities of He I and He II.

The qualitative behavior shown in Fig. 4 is indeed confirmed quantitatively, as the parameter $\langle \theta^2 \rangle$ increases with the oscillation frequency, in the range of investigated parameters. In other words, it is not surprising that, as the motion strength increases, the magnitude of the shed vortices also increases.

As it is customary in fluid dynamics, we present here our results on the vortex strength as a function of relevant Reynolds numbers, although we do not observe any strong oscillation amplitude dependence of the data. In the case of He I, we chose the (viscous) Reynolds number, as defined in Eq. (3).
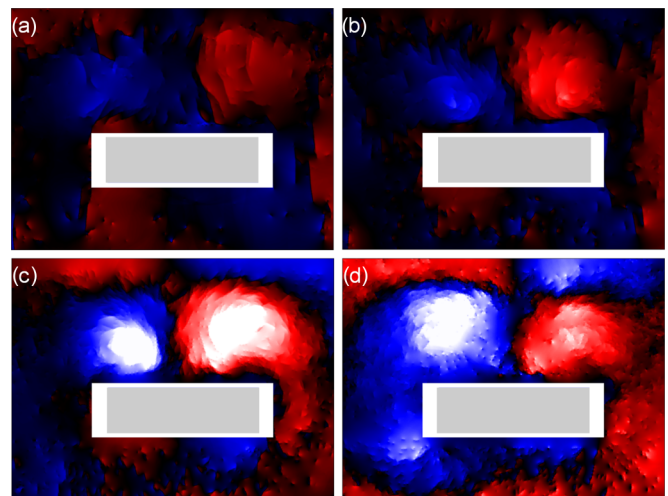

FIG. 4. (Color online) Maps of the $\theta(\mathbf{r}, \varphi)$ parameter, calculated at the lowest position of the oscillatory motion; amplitude $a = 5$ mm. (a) Frequency $f = 0.1$ Hz, temperature $T = 1.26$ K, Reynolds numbers $Re_n = 2443$ and $Re_\kappa = 1886$; (b) $f = 0.2$ Hz, $T = 1.26$ K, $Re_n = 4885$, and $Re_\kappa = 3771$; (c) $f = 0.5$ Hz and $T = 1.24$ K, see also the left panel of Fig. 2; (d) $f = 1$ Hz, $T = 1.24$, $Re_n = 23\,434$, and $Re_\kappa = 18\,855$. Legend as in Fig. 3.
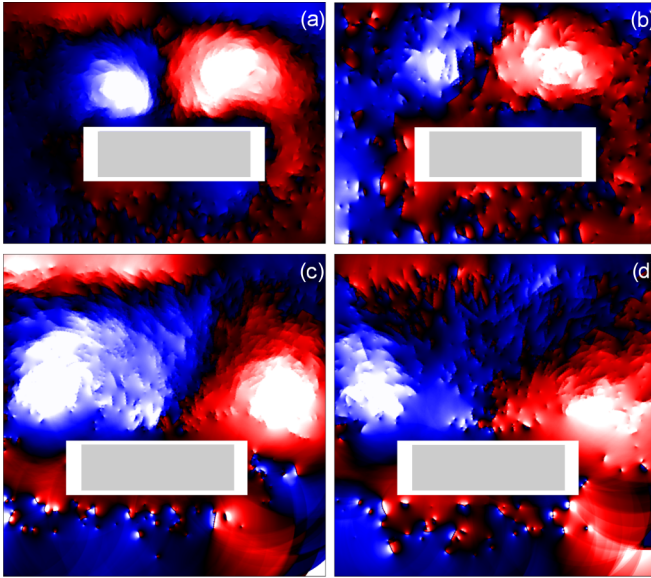
FIG. 5. (Color online) Maps of the $\theta(\mathbf{r},\varphi)$ parameter, calculated at the lowest position of the oscillatory motion; frequency $f = 0.5$ Hz. (a) He II, amplitude $a = 5$ mm and temperature $T = 1.24$ K, see also the left panel of Fig. 2; (b) He I, $a = 5$ mm and $T = 2.18$ K, see also the right panel of Fig. 2; (c) He II, $a = 10$ mm, $T = 1.40$ K, Reynolds numbers $Re_n = 29\,973$ and $Re_\kappa = 18\,855$; (d) He I, $a = 10$ mm, $T = 2.18$ K, and Reynolds number $Re = 18\,184$. Legend as in Fig. 3.

The corresponding Re range for our data lies approximately between 800 and 37 000 and the viscous penetration depth δ range, see again Eq. (3), is between about 0.25 mm, at the smallest Re, and 0.05 mm, being therefore always larger than our typical particle size, smaller than 0.01 mm.

For our He II data, the first (viscouslike) definition of Reynolds number we employ, see Eq. (4), leads to $900 < Re_n < 83\,000$ in the considered experimental conditions, which corresponds to δ ranging between approximately 0.23 and 0.04 mm, respectively.

Figure 6 displays the parameter $\langle \theta^2 \rangle$ as a function of these Reynolds numbers. The standard deviation σ of θ^2, normalized by $\langle \theta^2 \rangle$, is plotted, as a function of Re and Re_n, in the inset of Fig. 6, for the sake of clarity. It can be seen that σ can be up to eight times larger than the ensemble average of θ^2, that is, the data scatter cannot be neglected here. The He II data points shown in the main panel of Fig. 6 collapse to an increasing curve of the Reynolds number Re_n. Similarly, despite the larger scatter, the He I data points also display the tendency to collapse, but to another curve. The existence of these two separate curves, which is also consistent with the $\theta(\mathbf{r},\varphi)$ results reported above, is a puzzling outcome and we will attempt to provide possible physical explanations in the following section.

The second (superfluid) definition of Reynolds number we use here to characterize the obtained He II data, see Eq. (5), follows, as mentioned above, from the recent study by L'vov *et al.* [30] and, more generally, from the concept of effective kinematic viscosity ν_{eff}, introduced by Vinen [37]. It is assumed that the energy decay rate ϵ of the flow is proportional to the square of the quantized vortex length L
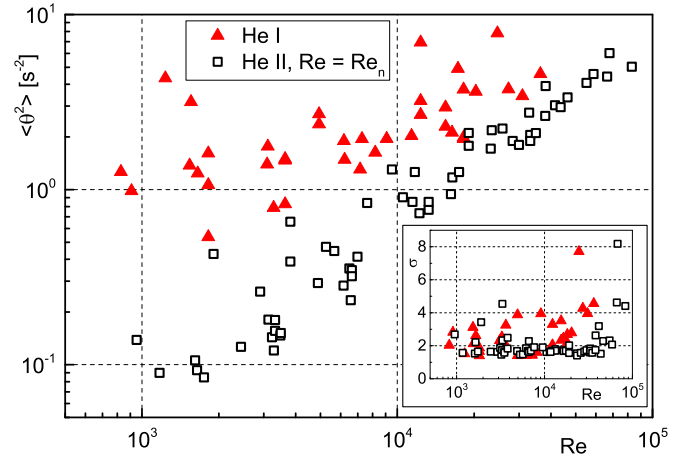

FIG. 6. (Color online) Parameter $\langle \theta^2 \rangle$ as a function of the Reynolds numbers Re and Re_n. Red triangles: He I. Open black squares: He II. (Inset) Normalized standard deviation σ of θ^2 as a function of Re and Re_n; symbols as in the main panel.

per unit volume, also known as the vortex line density, i.e.,

$$\epsilon = \nu_{\mathrm{eff}}(\kappa L)^2. \tag{8}$$

Although Eq. (8) lacks a rigorous theoretical justification, being mainly motivated by the analogy with the classical relation linking ϵ with the flow average vorticity, $\epsilon = \nu \Omega^2$, it has been successfully used to describe various He II flows. For example, as recently discussed by Varga *et al.* [38], mechanically generated flows of He II can, on large enough scales, be viewed as flows of a single-component fluid possessing an effective kinematic viscosity, which one can deduce from either temporal decay [39,40] or steady-state data [29]. Within the temperature range of the present study, ν_{eff} is weakly temperature dependent and its numerical value is known within a factor of 5 [29]. On the other hand, the fluid kinematic viscosity ν in He I, above the superfluid transition, is known and tabulated in Ref. [3] with sufficient accuracy. In
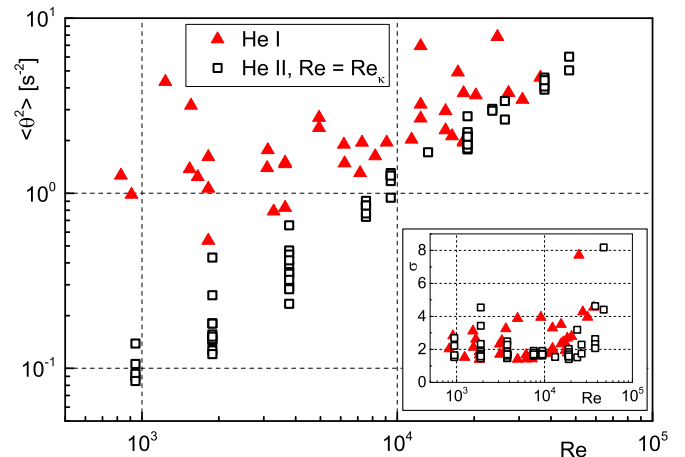

FIG. 7. (Color online) Parameter $\langle \theta^2 \rangle$ as a function of the Reynolds numbers Re and Re_κ. Red triangles: He I, as in Fig. 6. Open black squares: He II. (Inset) Normalized standard deviation σ of θ^2 as a function of Re and Re_κ; symbols as in the main panel.

Ref. [30], L'vov *et al.* derived that in He I, just above T_λ, the fluid kinematic viscosity ν can be set equal to approximately $\kappa/6$. Taking into account that the fluid kinematic viscosity ought to smoothly follow the temperature dependence of ν in He I across T_λ, we decided to use the value $\nu = \kappa/6$ for calculating the relevant (superfluid) Reynolds number in He II, see Eq. (5). We find that, in the present case, $900 < Re_\kappa < 48\,000$, corresponding to the δ range between about 0.23 and 0.05 mm, respectively. The behavior of $\langle\theta^2\rangle$ as a function of Re and Re_κ is shown in Fig. 7 and is qualitatively similar to that displayed in Fig. 6.

V. DISCUSSION

The most striking outcome reported above, see Figs. 6 and 7, is that the parameter $\langle\theta^2\rangle$ appears to behave differently in He I and He II, as a function of the Reynolds number, being therefore in contrast with the common assumption that forced flows of He II, at large enough length scales, are similar to viscous flows of comparable magnitude, as discussed, e.g., by Van Sciver *et al.* [9,34].

First of all, we note that particle velocity distributions in thermal counterflow are characterized by tails wider than in viscous flows, see, e.g., Ref. [10]. However, the present He II data do not display a larger scatter, in comparison with the He I data, as shown in the insets of Figs. 6 and 7. The behavior can be partly explained by the fact that, for some movies, the total number of trajectory points might not be sufficient to perform meaningful statistical calculations. In order to check this, we decided to keep only movies that, once processed, resulted in at least 40 000 trajectory points. The corresponding outcome is shown in Fig. 8, where we additionally averaged the data points obtained at the same Reynolds numbers, Re and Re_κ. The resulting $\langle\theta^2\rangle$ behavior is similar to that displayed in Fig. 7,
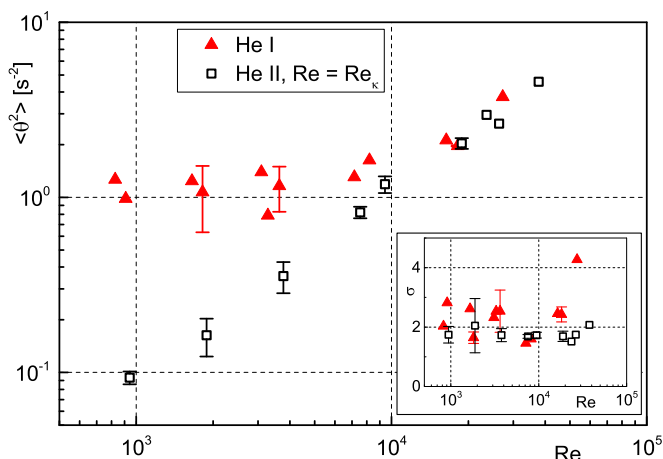

FIG. 8. (Color online) Parameter $\langle\theta^2\rangle$ as a function of the Reynolds numbers Re and Re_κ. Red triangles: He I. Open black squares: He II. Each experimental condition is represented by at least 40 000 track points. At each Reynolds number the corresponding average of the obtained $\langle\theta^2\rangle$ values is plotted; the shown error bars denote the standard deviation of the $\langle\theta^2\rangle$ values obtained at that Reynolds number. (Inset) Normalized standard deviation σ of θ^2 as a function of Re and Re_κ; symbols as in the main panel.

with a smaller scatter, σ being in this case up to five times larger than $\langle\theta^2\rangle$, instead than up to eight times.

If the data shown in Fig. 6 are filtered in the same fashion, that is, if data sets that represent less than 40 000 trajectory points are removed, the corresponding $\langle\theta^2\rangle$ trends do not change appreciably. Note, however, that, for given values of temperature T, frequency f and amplitude a, $Re_n > Re_\kappa$, as μ_n/ρ is smaller than $\kappa/6$, in the range of investigated parameters. In other words, the collapse of the two curves, at large Reynolds numbers, is less evident if Re_n is used to characterize the He II data.

The existence of two distinct branches, at Reynolds numbers smaller than approximately 10^4, but not above this value, although influenced by the relatively large data scatter, calls therefore for plausible physical explanations, not related to the used data processing procedure. Let us then speculate what physical aspects might lead to the observed result.

One of the most relevant differences between He I and He II is the fact that the heat conductivity of He II is about 10^6 times larger than that of He I [3], i.e., heat dissipates in He II at a much faster rate than in He I. If we take into account the parasitic heat to the experimental volume, due to the oscillating obstacle and to the laser sheet, we may say that, in He I, this heat is dissipated at a much slower rate than in He II, resulting in parasitic flows that might partly mask the macroscopic vortices shed at the cylinder edges, especially at the lowest frequencies. We estimate that the mechanical power due to the obstacle oscillations is of the order of 1 mW, roughly the same as the laser power absorbed by the cylinder, as previously calculated in Ref. [33]. It follows therefore that both phenomena may affect the resulting behavior of the liquid, especially He I, as in He II (where dissipation of the parasitic heat is very effective) particle trajectories appear not to be appreciably influenced by the laser heat input, in the absence of other flows, i.e., during free fall.

Another reason that might contribute to explain the obtained two curves at low Reynolds numbers is related to the fact that, as mentioned above, we have to date implicitly assumed that the probed length scale d is, in He II, of the same order as the average distance ℓ between quantized vortices (the quantum length scale). The probed length scale d can be viewed, both in He I and He II, as the average distance traveled by a particle between two consecutive frames. If we assume, for the sake of simplicity, that the average particle velocity is of the order of the imposed cylinder velocity, we find that d can be estimated as $d \approx \omega a/100$ (the movies were taken at 100 fps).

On the other hand, following, e.g., Eq. (8), we can write that the average vorticity due to the flow of He II is

$$\Omega \approx \kappa L = \frac{\kappa}{\ell^2}. \tag{9}$$

If we additionally assume that $\Omega^2 \approx \langle\theta^2\rangle$, an expression for estimating the average distance between quantized vortices is obtained as

$$\ell \approx \left(\frac{\kappa^2}{\langle\theta^2\rangle}\right)^{1/4}. \tag{10}$$

In order to compare the He I and He II data, let us now estimate a relevant flow length scale in viscous He I. It is natural to use the Kolmogorov scale and, by assuming $\Omega^2 \approx \langle\theta^2\rangle$, we
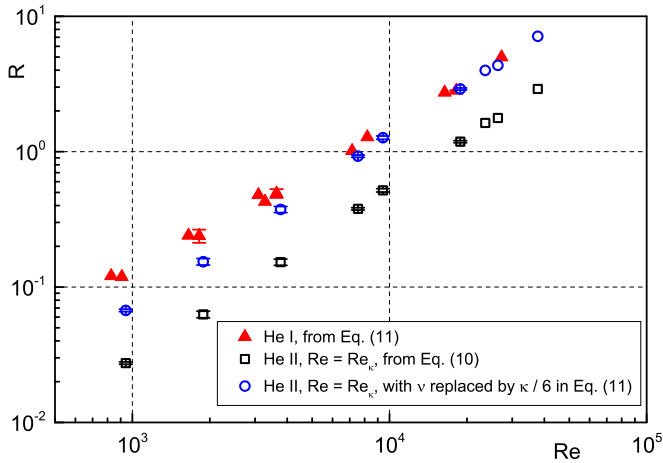
FIG. 9. (Color online) Ratio R between the probed length scale d and the flow scale s as a function of the Reynolds numbers Re and Re_κ. Red triangles: He I, with $s = \eta$, the Kolmogorov length scale, Eq. (11). Open black squares: He II, with $s = \ell$, the quantum length scale, Eq. (10). Open blue circles: He II, with $s = \ell$ calculated in the same fashion as η, i.e., ν is replaced by $\kappa/6$ in Eq. (11). Each experimental condition is represented by at least 40 000 track points. At each Reynolds number, the corresponding average of the obtained R values is plotted; the shown error bars denote the standard deviation of the R values obtained at that Reynolds number. See the text for further details on the used scales.

arrive at

$$\eta = \left(\frac{\nu^3}{\epsilon} \right)^{1/4} \approx \left(\frac{\nu^2}{\langle \theta^2 \rangle} \right)^{1/4}, \qquad (11)$$

where $\epsilon \approx \nu \langle \theta^2 \rangle$ is the energy dissipation rate, see again Eq. (8).

We can now define the ratio $R = d/s$, where $s = \ell$ (He II) and $s = \eta$ (He I). We find that, in the range of investigated parameters, 0.01 mm $< d <$ 0.48 mm and 0.09 mm $< \eta <$ 0.16 mm, for the He I data, and that 0.01 mm $< d <$ 0.63 mm and 0.21 mm $< \ell <$ 0.59 mm, for the He II data (each experimental condition is represented by at least 40 000 trajectory points and our particles are typically smaller than 0.01 mm).

The resulting ratio R is plotted in Fig. 9 as a function of Re and Re_κ. It is apparent that we are actually probing length scales larger than the relevant flow scale only at Reynolds numbers larger than about 10^4. In other words, the two branches displayed in Fig. 8 might possibly be due to the fact that, at Reynolds numbers smaller than 10^4, we are investigating scales smaller than the dissipative flow scale, in He I, and the quantum length scale, in He II. While in He I, below the Kolmogorov length scale, the fluid motion is dissipated into heat by the action of the finite viscosity, quantum flows of He II may exist all the way down to the Å scale—the size of the cores of quantized vortices. We may say that quantum restrictions on the superfluid motion could be the reason why, for Reynolds numbers smaller than 10^4, the parameter $\langle \theta^2 \rangle$ behaves differently in He I and He II.

The outcome can also be seen as a further experimental support of the concept of effective kinematic viscosity of He II, as we simply set the kinematic viscosity of He II equal to

that of He I just above T_λ, which is 1.66×10^{-8} m^2/s. Indeed, if ν is substituted by $\kappa/6$ in Eq. (11), we obtain values of R closer to the viscous values, especially at Reynolds numbers larger than 10^4. Additionally, we may argue that, in the present case, the average flow vorticity might not solely result from the action of quantized vortices, as postulated in Eq. (8).

To summarize, we have identified and discussed three possible reasons why the parameter $\langle \theta^2 \rangle$ at low Reynolds numbers behaves differently in He I and He II, namely the data scatter, different heat conductivities of He I and He II, and the fact that the probed length scales are smaller than the Kolmogorov scale, in He I, and the quantum length scale, in He II.

VI. CONCLUSIONS

The behavior of macroscopic, millimeter-sized vortical structures, generated by a sharp-edged body oscillating in liquid ^{4}He, was studied by visualizing the dynamics of micrometer-sized particles seeding the fluid. A cylinder of rectangular cross section (3 mm high and 10 mm wide) performed quasiharmonic oscillations in the liquid, at various frequencies (ranging between 0.05 and 1.25 Hz) and amplitudes (5 and 10 mm), at temperatures between about 1.2 and 3 K, resulting in Reynolds numbers up to 10^5. Consequently, in the present experiments, a direct comparison between similar, mechanically driven flows of He I, a viscous Newtonian fluid, and He II, a liquid displaying superfluidity, was carried out.

First of all, our visualization study confirms the existence of large vortical structures shed by the oscillating body, which appear similar in viscous He I and superfluid He II. Although this result is not surprising (for example, as already mentioned, visualization of macroscopic vortex rings was reported by Murakami *et al.* [19] in 1987 and by Stamm *et al.* [20] in 1994), our investigation represents, to the best of our knowledge, the first systematic visualization study of quantum flows due to an oscillating object. We note, additionally, that in viscous fluids vortices are shed by accelerating plates at similar Re as the minimum Reynolds numbers investigated here, as reported by Taneda and Honji [25].

In order to characterize the magnitude of the shed vortices, we introduced the parameter $\langle \theta^2 \rangle$, which is loosely related to the flow vorticity and can be interpreted as the square of the vorticity magnitude, characteristic for a particular phase interval of the harmonic motion, coarse-grained over a suitable circular area. At Reynolds numbers lower than approximately 10^4, a noticeable difference between the investigated He I and He II flows is observed. More precisely, after thorough studies of the quality of the data sets and of the robustness of the processing procedure, we found that the probed length scales are, at these low Reynolds number, smaller than the quantum (dissipative) scale of the flow, determined, in He II, by the average distance between quantized vortices and, in He I, by the Kolmogorov dissipative scale. For Reynolds numbers larger than 10^4, the effect vanishes and He II behaves similarly to He I, as it is expected for mechanically driven flows of superfluid ^{4}He at length scales exceeding the average distance between quantized vortices. This suggests that, similarly to thermal counterflow [10,11], both viscous and quantum features can be observed in mechanically driven flows of He

II, depending on the length scales at which the quantum flow is probed.

Note, however, that the observed effect might also be influenced by the much larger thermal conductivity of He II, compared to that of He I, leading to different dissipation mechanisms of the parasitic energy input. Additionally, the obtained $\langle \theta^2 \rangle$ values are affected by the data scatter, which cannot be neglected here. In order to clarify the reported behavior, future studies should therefore be devoted to increase the data set size, as this will likely lead to less uncertainty in the evaluation of the various physical quantities of interest, such as the introduced $\langle \theta^2 \rangle$ parameter. Nevertheless, the employed visualization technique appears capable of providing meaningful physical insight into the investigated problem and, in

particular, seems suitable to study the occurrence of cavitation in the proximity of fast oscillating objects, such as quartz tuning forks [14], or the detailed mechanisms of shedding and subsequent dynamics of large-scale vortical structures in superfluid He II.

[1] L. Skrbek and K. R. Sreenivasan, Phys. Fluids **24**, 011301 (2012).

[2] C. F. Barenghi, L. Skrbek, and K. R. Sreenivasan, Proc. Natl. Acad. Sci. USA **111**, 4647 (2014).

[3] R. J. Donnelly and C. F. Barenghi, J. Phys. Chem. Ref. Data **27**, 1217 (1998).

[4] W. Guo, M. La Mantia, D. P. Lathrop, and S. W. Van Sciver, Proc. Natl. Acad. Sci. USA **111**, 4653 (2014).

[5] M. S. Paoletti, M. E. Fisher, K. R. Sreenivasan, and D. P. Lathrop, Phys. Rev. Lett. **101**, 154501 (2008).

[6] M. La Mantia, T. V. Chagovets, M. Rotter, and L. Skrbek, Rev. Sci. Instrum. **83**, 055109 (2012).

[7] M. La Mantia, D. Duda, M. Rotter, and L. Skrbek, J. Fluid Mech. **717**, R9 (2013).

[8] G. P. Bewley, M. S. Paoletti, K. R. Sreenivasan, and D. P. Lathrop, Proc. Natl. Acad. Sci. USA **105**, 13707 (2008).

[9] T. V. Chagovets and S. W. Van Sciver, Phys. Fluids **27**, 045111 (2015).

[10] M. La Mantia and L. Skrbek, Europhys. Lett. **105**, 46002 (2014).

[11] M. La Mantia and L. Skrbek, Phys. Rev. B **90**, 014519 (2014).

[12] W. F. Vinen and L. Skrbek, in *Progress in Low Temperature Physics: Quantum Turbulence*, edited by M. Tsubota and W. P. Halperin (Elsevier, Amsterdam, 2009), pp. 195–246.

[13] W. F. Vinen and L. Skrbek, Proc. Natl. Acad. Sci. USA **111**, 4699 (2014).

[14] M. Blažková, D. Schmoranzer, and L. Skrbek, Low Temp. Phys. **34**, 380 (2008).

[15] D. Schmoranzer, M. Kráľová, V. Pilcová, W. F. Vinen, and L. Skrbek, Phys. Rev. E **81**, 066316 (2010).

[16] E. Zemma and J. Luzuriaga, J. Low Temp. Phys. **173**, 71 (2013).

[17] E. Zemma, M. Tsubota, and J. Luzuriaga, J. Low Temp. Phys. **179**, 310 (2015).

[18] M. Blažková, M. Človečko, V. B. Eltsov, E. Gažo, R. de Graaf, J. J. Hosio, M. Krusius, D. Schmoranzer, W. Schoepe, L. Skrbek, P. Skyba, R. E. Solntsev, and W. F. Vinen, J. Low Temp. Phys. **150**, 525 (2008).

[19] M. Murakami, M. Hanada, and T. Yamazaki, Jpn. J. Appl. Phys. **26**, Suppl. 26-3, 107 (1987).

[20] G. Stamm, F. Bielert, W. Fiszdon, and J. Piechna, Physica B **193**, 188 (1994).

[21] T. Zhang and S. W. Van Sciver, Nat. Phys. **1**, 36 (2005).

[22] C. H. K. Williamson, Annu. Rev. Fluid Mech. **28**, 477 (1996).

[23] M. La Mantia and P. Dabnichki, Eng. Anal. Bound. Elem. **35**, 404 (2011).

[24] A. W. Mackowski and C. H. K. Williamson, J. Fluid Mech. **765**, 524 (2015).

[25] S. Taneda and H. Honji, J. Phys. Soc. Jpn. **30**, 262 (1971).

[26] L. Tao and K. Thiagarajan, Appl. Ocean Res. **25**, 21 (2003).

[27] C. N. Phan, M. Aureli, and M. Porfiri, J. Fluids Struct. **40**, 52 (2013).

[28] G. H. Keleugan and L. H. Carpenter, J. Res. Natl. Bur. Stand. **60**, 423 (1958).

[29] S. Babuin, E. Varga, L. Skrbek, E. Lévêque, and P.-E. Roche, Europhys. Lett. **106**, 24006 (2014).

[30] V. S. L'vov, L. Skrbek, and K. R. Sreenivasan, Phys. Fluids **26**, 041703 (2014).

[31] H. W. Woolley, R. B. Scott, and F. B. Brickwedde, J. Res. Natl. Bur. Stand. **41**, 379 (1948).

[32] S. C. Bates, *Compilation of the Engineering Properties of Solid Hydrogen* (Thoughtventions, Glastonbury, CT, 2002).

[33] D. Duda, M. La Mantia, M. Rotter, and L. Skrbek, J. Low Temp. Phys. **175**, 331 (2014).

[34] T. Xu and S. W. Van Sciver, Phys. Fluids **19**, 071703 (2007).

[35] I. F. Sbalzarini and P. Koumoutsakos, J. Struct. Biol. **151**, 185 (2005).

[36] D. Duda, M. La Mantia, and L. Skrbek, in *WDS'14 Proceedings of Contributed Papers - Physics*, edited by P. Šafránková and J. Pavlů (Matfyzpress, Prague, 2014), pp. 73–78.

[37] W. F. Vinen, Phys. Rev. B **61**, 1410 (2000).

[38] E. Varga, S. Babuin, and L. Skrbek, Phys. Fluids **27**, 065101 (2015).

[39] T. V. Chagovets, A. V. Gordeev, and L. Skrbek, Phys. Rev. E **76**, 027301 (2007).

[40] L. Skrbek and K. R. Sreenivasan, in *Ten Chapters in Turbulence*, edited by P. A. Davidson, Y. Kaneda, and K. R. Sreenivasan (Cambridge University Press, Cambridge, 2013), pp. 405–437.